Tidal turbine benchmarking project: Stage I - steady flow experiments

S.W. Tucker Harvey, X. Chen, D.T. Rowe, J. McNaughton, C.R. Vogel, K. Bhavsar, T. Allsop, J. Gilbert, H. Mullings, T. Stallard, I. Benson, A. Young, & R.H.J. Willden

Abstract—**The tidal turbine benchmarking project, funded by the UK's EPSRC and the Supergen ORE Hub, has conducted a large laboratory scale experiment on a highly instrumented 1.6 m diameter tidal rotor. The turbine is instrumented for the measurement of spanwise distributions of flapwise and edgewise bending moments using strain gauges and a fibre Bragg optical system, as well as overall rotor torque and thrust. The turbine was tested in well-defined flow conditions, including grid-generated freestream turbulence, and was towed through the 12.2 m wide, 5.4 m deep long towing tank at Qinetiq's Haslar facility. The turbine scale was such that blade Reynolds numbers were $\mathbf{Re} = \mathbf{3 \times 10^5}$ and therefore post-critical, whilst turbine blockage was kept low at 3.0%.**

In order to achieve higher levels of freestream turbulence a 2.4 m by 2.4 m turbulence grid was towed 5 m upstream of the turbine. Measurements to characterise the grid generated turbulence were made at the rotor plane using an Acoustic Doppler Velocimeter and a five-hole pressure probe. An elevated turbulence of 3.1% with homogeneous flow speed across the rotor plane was achieved using the upstream turbulence grid.

The experimental tests are well defined and repeatable, and provide relevant data for validating models intended for use in the design and analysis of full-scale turbines. This paper reports on the first experimental stage of the tidal benchmarking programme, including the design of the rotor and comparisons of the experimental results to blade resolved numerical simulations.

Index Terms—**Tidal stream turbine, Towing tank experiments, Benchmarking, Turbine fluid mechanics, Turbulence generation.**

I. Introduction

The development of renewable energy generation technologies has become a key focus in the response to climate change. Tidal stream energy represents an underutilised renewable energy resource with the benefits of high predictability and availability, however current installation is limited, with order 10's MW installed capacity worldwide. Although promising, the sector faces difficult challenges, ranging from issues relating to survivability and maintenance, to environmental considerations. Yet it is the bounds of the understanding of the complex fluid mechanics that govern tidal turbines that have created some of the greatest challenges. Tidal turbines operate in hostile hydrodynamic environments, dominated by unsteady flow phenomena related to waves, shear, turbulence and platform motion, in the case of floating devices. Current modelling methodologies are often unable to accurately capture these flow effects, leading to uncertainty in turbine loading and conservatism in design through low confidence in model predictions. To reduce the uncertainties of these mathematical and engineering models, large-scale experimental data are required to enable model validation.

A number of experimental investigations of tidal turbines have been completed, ranging from simple cases such as a single turbine in uniform flow conditions, [1]–[3], to more complex conditions, with elevated turbulence [4], waves and shear [5] and multiple turbines interacting. Yet few of these studies have led to the generation of well-documented datasets that can be utilised for model validation, especially at scales large enough to obtain Reynolds number independence and hence comparability to full-scale devices. Further, blockage at small laboratory scales often obscures test results, and recorded data is often limited to whole rotor loads which can be of limited use for model validation, particularly in unsteady flows.

The tidal turbine unsteady benchmarking project, funded by the UK's EPSRC and the Supergen Offshore Renewable Energy Hub, has conducted a large laboratory scale experiment on a highly instrumented 1.6m diameter tidal rotor. The turbine was tested in a large towing tank providing low blockage. It was instrumented for the measurement of the spanwise distributions of the flapwise and edgewise bending moments and tested in well-defined flow conditions, including elevated freestream turbulence. The testing was followed by a blind benchmarking exercise, in which engineers from both academia and industry were invited to submit predictions of the turbine loading under various flow conditions. The comparison of the submitted simulation results and the experimental measurements has improved the understanding of the limitations of the different modelling methodologies submitted and aided in their development.

In this paper, we present the experimental results of the tidal benchmarking project, as an open source data set to aid future model validation. The results of the benchmarking exercise are reported [6]. In this

Authors S.W. Tucker Harvey, X. Chen, D. Rowe, J. McNaughton, C.R Vogel and R.H.J. Willden are affiliated with the Department of Engineering Science, University of Oxford (e-mail: richard.willden@eng.ox.ac.uk).

Authors K. Bhavsar, T. Allsop and J. Gilbert are affiliated with the Faculty of Science and Engineering, University of Hull.

Authors T. Stallard and H. Mullings are affiliated with the Department of Mechanical, Aerospace and Civil Engineering, University of Manchester.

Authors I. Benson and A. Young are affiliated with the Department of Mechanical Engineering, University of Bath.

Digital Object Identifier:
https://doi.org/10.36688/ewtec-2023-553

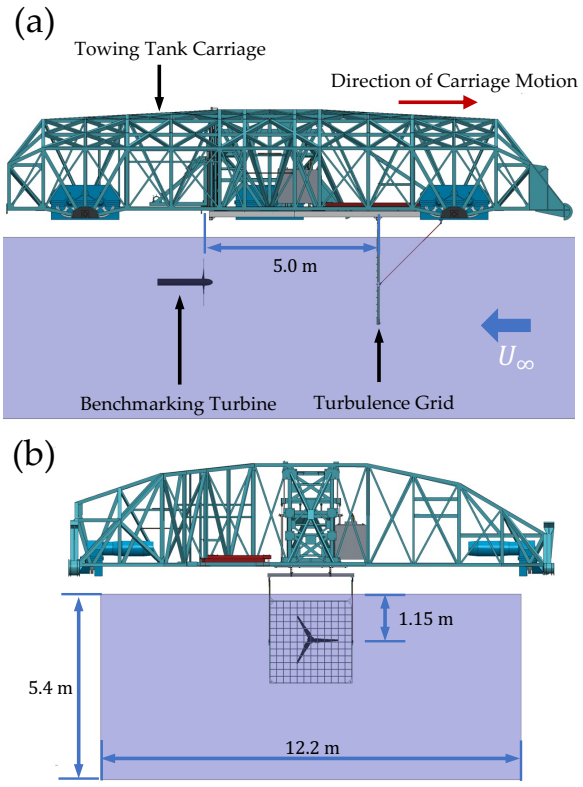

Fig. 1. Illustration of experimental setup in the Haslar towing tank. (a) Shows a side view of the towing tank carriage, whilst the view from behind the carriage (looking upstream) is shown in (b).

paper, we begin with a description of the experimental facility and test conditions in section II. Following this, in section III, the hydrodynamic design process utilised for the development of the benchmarking turbine is outlined with comparison to some of the experimental results. This leads into the detailed mechanical design and instrumentation of the benchmarking turbine, which are discussed in section IV. Following a discussion of data processing in section V, the results, including the time averaged integrated variables and unsteady loading spectra, are presented and discussed in section VI.

II. Facility Selection and Test Conditions

To maximise the utility of the benchmarking dataset we sought to operate a turbine at as high a Reynolds number as possible, with minimum flow blockage in realistic flow conditions - turbulence and waves. While both field testing and laboratory flume turbine experiments offer the prospect of obtaining these conditions to vary extents, towing tank facilities provide the benefits of a highly uniform inflow and closely controlled flow velocity, as well as a large cross section and hence low blockage. These benefits and the resultant repeatability led to the QinetiQ towing tank facility based in Haslar, Portsmouth, being selected for the tidal turbine benchmarking testing. With a width of $12.2\,\mathrm{m}$ and depth of $5.4\,\mathrm{m}$, a low global blockage can be obtained even with a relatively large test turbine; blockage of $3.05\,\%$ by area for a $1.6\,\mathrm{m}$ diameter turbine. Figure 1 illustrates the experimental setup within the Haslar facility at QinetiQ. The test turbine has a diameter, D, of $1.6\,\mathrm{m}$, and was designed for a tip-speed ratio, λ, of 6.0 so as to achieve a post-transitional Reynolds number of between $250\mathrm{k} \rightarrow 300\mathrm{k}$. A relatively large diameter also allowed for in-blade instrumentation.

Due to their nature, the level of freestream turbulence in towing tank facilities is very low. Hence, to raise this value for an elevated turbulence test case, a carriage-mounted turbulence grid was developed. The turbulence grid was $2.4\,\mathrm{m}$ by $2.4\,\mathrm{m}$ in size ($1.5D$ by $1.5D$) and had a porosity of 0.95. This was achieved using a grid of 13 horizontal and vertical bars of $15\,\mathrm{mm}$ width. The grid was mounted to the towing tank carriage upstream of the turbine as illustrated in figure 1. Prior to the experimental testing of the benchmarking turbine with the turbulence grid, the flow behind the grid was characterised with a Nortek Vectrino Acoustic Doppler Velocimeter (ADV). Additional measurements where acquired with the Barnacle 5 hole probe developed by [7], verifying the results obtained with the ADV. All measurements were obtained in the turbine rotor plane, which was located $5\,\mathrm{m}$ downstream of the turbulence grid. At this location the grid generated a relatively uniform onset flow to the rotor of $0.899\,\mathrm{m/s}$ when the carriage was towed at $1.0\,\mathrm{m/s}$, with an elevated turbulence level of 3.1%; see section VI for further details.

The turbine was tested with both the turbulence grid mounted in-front of the turbine and without it, providing an elevated and a low turbulence dataset. The rotor's angular velocity, ω, was varied so as to achieve a range of tip-speed ratios at the given tow speed. The rotor tip-speed ratio (TSR) is defined as,

$$\lambda = \frac{\omega R}{U_\infty} \tag{1}$$

where U_∞ is the onset flow speed and R the turbine radius. The tip-speed ratios for both the low turbulence (without turbulence grid) and elevated turbulence (with turbulence grid) cases are tabulated in table I. A finer spacing of angular velocities was used around the design tip speed ratio to ensure the peak coefficient of performance was well resolved. For all experiments a settling time of 15 minutes was used between tests and each test case was conducted three times to ensure repeatability and robustness of results. Further experiments with onset head waves, without the turbulence grid, have also been conducted to provide a further unsteady loading dataset. These will be the subject of a future benchmarking exercise.

III. Hydrodynamic Design

A. Hydrofoil Profile

The hydrodynamic design process of the benchmarking turbine starts with the selection of the hydrofoil profile. After careful investigation and comparisons across a selection of different hydrofoils employed by existing successful tidal turbines, the NACA 63-415 profile was selected for the benchmarking turbine. This profile, and its family variation 63-815, have been successfully used in a number of different laboratory tidal

TABLE I
DEFINITION OF TEST CONDITIONS.

Low Turbulence Cases											
Test No.	1	2	3	4	5	6	7	8	9	10	11
λ	4.02	4.52	5.03	5.53	5.78	6.03	6.28	6.53	7.04	7.54	7.87
Elevated Turbulence Cases											
Test No.	1	2	3	4	5	6	7	8	9	10	11
λ	4.01	4.57	5.03	5.50	5.78	6.06	6.34	6.52	7.08	7.55	7.92

turbines, such as the model test turbine used by [8] (now part of GE power), the MCT experimental tidal turbine built by [1] at the University of Southampton, and the X-MED experimental tidal turbine by [3] at the University of Manchester.

We use a single hydrofoil profile from hub to tip to construct the entire blade of the benchmarking turbine, without a root transition piece. This simplification to commercial blades, which operate much thicker sections towards the blade root for structural reasons, and root transition pieces for blade pitch control, is made for the benchmarking turbine to provide a simple-to-reproduce rotor. The desire for simplicity originates from modelling and interpretation issues that have been encountered in previous research involving different experimental and commercial turbines that uses multiple airfoil or hydrofoil profiles (e.g. [9], [10], [11]), as well as from the positive experiences of other research groups that have employed a single profile; [1] and [3]. It can be difficult for engineering and CFD models to accurately reproduce the exact geometries of the transitions between different foil sections, and coupled with this is the use of a compatible interpolation method for foil lift and drag data representing different sections. Hence, we use a single profile which avoids problems in the design process as well as enabling the benchmarking process to concentrate on the accuracy of flow modelling techniques rather than the interpretation and interpolation between different sections.

The trailing edge of the profile must be thickened from the profile's defined sharp trailing-edge due to both safety and manufacturing considerations. This must be achieved with care so as not to significantly alter the 2D hydrodynamic performance. One common approach to implementing this thickening is to truncate the profile ahead of the trailing edge at the desired trailing edge thickness-to-chord ratio and re-scale the profile to standard chord length. However this simple truncation method can result in significant changes to the hydrodynamic performance of the profile. Instead we adopt a trailing-edge thickening function from [12] which offers an alternative approach that adds thickness to both sides of the trailing section of the foil without altering the foil's camber line, and maintains its hydrodynamic performance. This thickening method has been successfully employed in Oxford's previous $1.2\,\mathrm{m}$ tidal turbine design in [13]. The equation of the thickening function is given as

$$y_t = \begin{cases} y_0 & 0 \le x \le x_T\,, \\ y_0 \pm 0.5\delta \left(\frac{x-x_T}{c-x_T}\right)^n & x_T \le x \le c\,, \end{cases} \qquad (2)$$

where x and y_0 denote the coordinates of the original sharp profile. y_t is the y coordinate of the thickened profile, which departs from the original profile downstream of an x coordinate value of x_T. Thickness is applied to both suction and pressure surfaces as indicated by $+/-$ respectively. The thickness at the trailing edge is represented by δ, chosen to be $0.00625c$ for the benchmarking blade profile, where c is the chord length. The parameter n defines the shape of the thickened section of the profile and was set to 2.0. A comparison between the thickened trailing edge, the truncated trailing edge and the original sharp profile is illustrated in Fig. 2.

The influence of the different thickening methods on the blade's hydrodynamic performance was investigated using two-dimensional Computational Fluid Dynamics (CFD) simulations using the RANS approach with SST $\mathrm{k}-\omega$ turbulence closure. Three profiles were investigated: the truncated profile, the trailing edge thickened profile and the original sharp trailing edge profile, with the first two profiles thickened to the same trailing edge thickness. The simulated lift and drag coefficients, as well as the resulting lift-to-drag ratio are presented in Fig. 3 (a), (b) and (c).

We make comparison to two sets of experimental data: the DTU wind tunnel tests by [14] at a blade chord Reynolds number of 1.6×10^6, and the USP test by [15] at $Re = 3.2 \times 10^5$, with the lower being representative of large laboratory experiments and the higher representative of field conditions. The lower Re experimental data exhibits lower lift, higher drag, and consequently lower lift-to-drag across the full range of angles of attack. In our simulations we consider two turbulence intensities, 1% and 8%, as the turbulence intensity in the frame of the blade increases from blade tip to root.

The simple truncated profile results in a significant reduction in lift as well as a more modest reduction in drag coefficient relative to the sharp trailing edge profile, which collectively lead to a reduction in the lift-to-drag ratio as well as a shift in the peak performance point (where maximum C_l/C_d occurs) towards a higher angle of attack, comparing to the sharp and thickened profiles. Meanwhile, the thickening function successfully maintains a close performance in both lift and drag compared to the sharp trailing edge profile. Using the thickening function to blunt the trailing edge is therefore advantageous as it provides flexibility in modelling approaches that may be employed in the later benchmarking phases; blade resolved investigations may choose to use a sharp trailing edge for efficiency, whilst models requiring sectional blade characteristics as input coefficients, such as Blade Element Momentum (BEM) or Actuator Line type simulations,

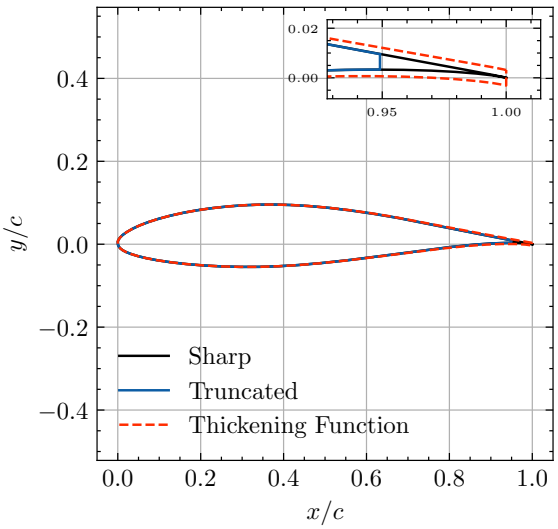

Fig. 2. Hydrofoil design: trailing edge treatment examples.

can utilise either sharp or thickened foil performance data with little modelling difference.

B. Blade Design

The rotor blades were designed using an in-house RANS Blade Element (RANS-BE) actuator disk type model embedded through a User Defined Function in Fluent, with the $k-\omega$ SST model used to provide turbulence closure. The model works to iteratively twist and taper the blades to achieve design angle of attack and loading distributions along each blade; further details of the method can be found in [13].

As stated in the test conditions, the turbine will be operating at a blockage ratio of 3.05% and was originally designed for an upstream turbulence intensity of $7 \sim 9\%$. The blockage ratio in the design simulations follows the channel blockage ratio, but within a cylindrical numerical domain. It is also found that the local turbulence intensity on the blade hydrofoil sections has a large influence on their hydrodynamic performance, especially for the drag coefficient, as indicated by the different coloured lines in Fig. 3. Hence, the rotor design simulation also takes the blade local turbulence intensity into account, which offers an improvement in fidelity of prediction over more standard BEM and RANS-BE design approaches.

A design process was followed whereby the tip-speed ratio is set to a design value, $\lambda = 6.0$, with a target angle-of-attack of $6°$, which is close to the hydrofoil's optimal lift-to-drag ratio as Fig. 3 (c) illustrates. The blade twist and chord are then iteratively altered to achieve a target local thrust coefficient of $C_x(r) = 2.0$ along the entire length of the blade, where $C_x(r) = T(r)/\frac{1}{2}\rho U_x^2\, 2\pi r$, and $T(r)$ is the thrust per unit span, U_x is the axial flow velocity at the rotor plane, ρ is the fluid density and r the radial coordinate. Note that $C_x(r)$ is relieved smoothly to 1.0 as the hub is approached in order that the solidity is not excessive in this region; see Fig. 5 (a). The resulting blade design, chord length and twist distribution, for the benchmarking rotor are presented in Fig. 4. The rotor is designed to have 3 blades and a nacelle diameter of $0.2\,\mathrm{m}$ $(0.125R)$ to accommodate the drive-train and instrumentation.

Following the iterative design process, confirmatory steady flow blade-resolved simulations were carried out using a RANS $k-\omega$ SST model with a multiple-reference frame (MRF) method on a $120°$ wedge cylindrical domain containing a single blade of the three bladed rotor. The mesh contains 38 million cells with a wall $y^+ \sim 1$. The simulations were run at the same blockage ratio as the rotor design process and the experiment, and across a range of tip-speed ratios around the design condition. The aim of these simulations was to validate the rotor performance and study the hydrodynamic effects that are difficult to measure experimentally. Interrogating the blade resolved simulation results leads to the computed loading distributions and angles of attack presented in Fig. 5, with simulated rotor performance discussed later in Fig. 10 and 11. Further details of the accompanying CFD study will be presented in a future publication.

Observing the simulated rotor loads it is seen that the design angle of attack is undershot by around $0.3°$ or less across most of the blade span, with greater departures at the blade root and tip, whilst the blade local thrust coefficient is well matched except in the tip region. The difference here is due to tip-loss effects which are not modelled in the RANS-BE design process due to iterative stability constraints.

IV. Mechanical Design and Instrumentation

The benchmarking turbine was extensively instrumented, with the instrumentation largely driving the mechanical design. This led to an elongated nacelle with a length of $2.4\,\mathrm{m}$ to incorporate the required instrumentation and electronics, as illustrated in figure 6. A servo motor provided by Moog Ltd was employed for the generator due to its capability to maintain constant angular velocity even with substantially varying load, while a 16:1 planetary gearbox enabled the motor to match the power and angular velocity requirements of the turbine.

The primary measurements obtained in most turbine experiments are the rotor torque and thrust. For the benchmarking turbine, these were measured by a shaft-mounted Torque/Thrust transducer provided by Applied Measurements Ltd. By positioning this sensor at the upstream end of the drive-train, and ahead of the front bearing, the influence of mechanical losses generated by the bearings and other drive-train components were excluded from measurements. Further to whole rotor measurements, individual blade loads were evaluated by both in-blade sensors and an instrumented hub section. Two of the three blades were instrumented with strain gauges positioned along the blade span, while all three of the blade roots provided both edgewise and flapwise root bending moments. The third blade was instrumented with Fibre Bragg grating (FBG) sensors, with the required acquisition electronics mounted within the nosecone of the turbine,

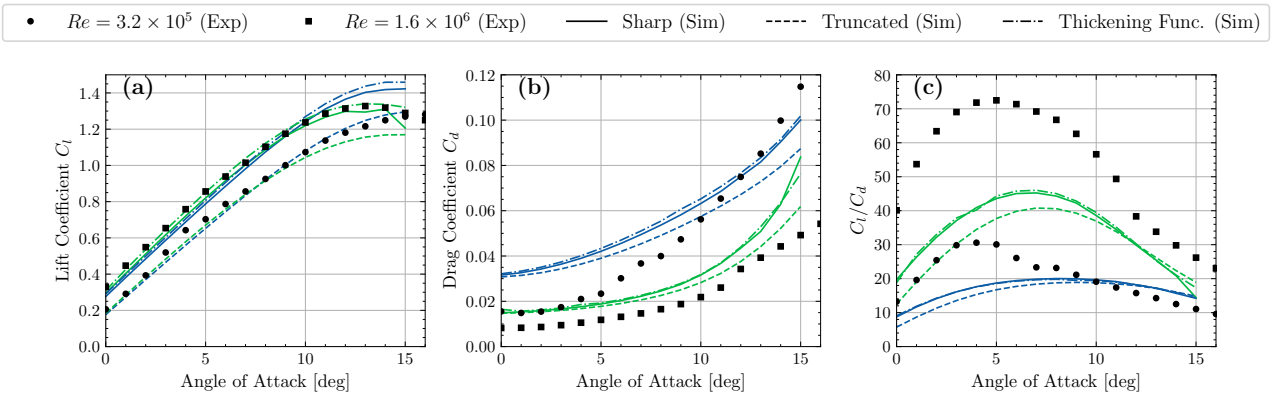

Fig. 3. Lift (a), drag (b) coefficients and lift-to-drag ratio (c) for the NACA 63-415 hydrofoil for different trailing edge treatments, together with experimental measurements. Line colour infers turbulence level; blue is $Tu = 8\%$, green is $Tu = 1.3\%$.

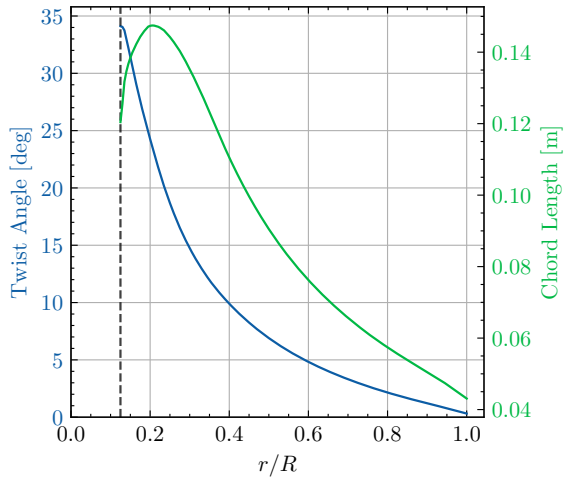

Fig. 4. Blade design: chord length (green) and twist angle (blue) distributions, the vertical dashed line indicates the nacelle diameter.

however these were not operated during this set of experiments. In addition to the load measurements, the angular position of the rotor was tracked by a rotary encoder positioned at the downstream end of the shaft. All signals were acquired with a sampling frequency of 200 Hz.

To enable instrumentation to be positioned within the blades, each blade was constructed from two machined aluminium components, which were bonded together. By adhering the two parts together, an instrumentation channel was created, which was designed to twist and taper with the blade profile providing internal faces equidistant from the blade's neutral axis and aligned with the local chordwise and chord-normal directions. The locations of the strain gauges within the channel are shown in Fig 7 (a). The first signal, which was more sensitive to loading in the edgewise direction, was created with the gauges in positions A and B, whilst the second signal, which was more sensitive to the flapwise direction, was created with gauges in positions C and D. Using a bench calibration procedure, the two signals were linearly mapped to their corresponding bending moments in the edgewise and flapwise directions. In the radial direction, the sensor locations were not equally spaced, with closer spacing at the hub and tip regions. Fig. 7 (b) shows the radial locations of the in-blade sensors, as well as the radial position of the root bending sensor.

V. Data Processing

A. Flow Data

Flow data acquired with ADV probes is often highly influenced by noise and erroneous spikes, hence care is required in the selection of processing methodologies applied prior to calculation of turbulence statistics. The despiking algorithm developed by [16] was found to effectively remove the high level of spikes in the raw dataset, while the influence of Doppler noise in the turbulence intensities and integral lengthscales was accounted for by the methodology described by [17]. The turbulence intensities are defined as,

$$i_x = \frac{\left(\overline{u'^2}\right)^{\frac{1}{2}}}{(\bar{u}^2+\bar{v}^2+\bar{w}^2)^{\frac{1}{2}}}, \quad i_y = \frac{\left(\overline{v'^2}\right)^{\frac{1}{2}}}{(\bar{u}^2+\bar{v}^2+\bar{w}^2)^{\frac{1}{2}}} \quad \text{and} \quad i_z = \frac{\left(\overline{w'^2}\right)^{\frac{1}{2}}}{(\bar{u}^2+\bar{v}^2+\bar{w}^2)^{\frac{1}{2}}} \tag{3}$$

where u, v and w are the velocity components in the x, y and z directions and i_i denotes the turbulence intensity in the i^{th} direction, with overbars and primes indicating time means and fluctuating components. The integral lengthscales were computed using the temporal auto-correlation function, defined as,

$$R_{xx}(\tau) = \frac{\overline{u'(t)u'(t+\tau)}}{\overline{u'(t)u'(t)}}, \tag{4}$$

where R_{xx} denotes the autocorrelation function for the u velocity component and τ is a time lag, with similar expressions written for the v and w velocity components. Considering Taylor's frozen turbulence hypothesis [18], the integral lengthscale can be estimated by integrating the autocorrelation,

$$\Lambda_x = \bar{u} \int_0^\infty R_{xx}(\tau)\, d\tau, \tag{5}$$

where Λ_x denotes the integral lengthscale for the u velocity component. Following the analysis of [19], and in a similar fashion to other tidal experiments [20], the integral was evaluated using the first zero crossing of the autocorrelation function as an upper limit to τ.

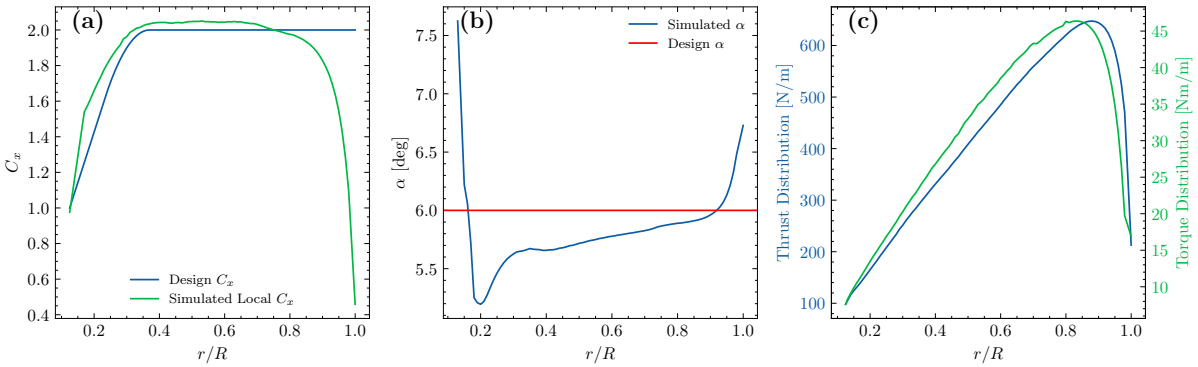

Fig. 5. Blade design parameters. (a) and (b) show spanwise variations of the design targets, local thrust coefficient C_x and angle-of-attack α, together with the values from the performance CFD simulation. (c) shows simulated thrust and torque distributions. All results shown are at the design tip-speed ratio.

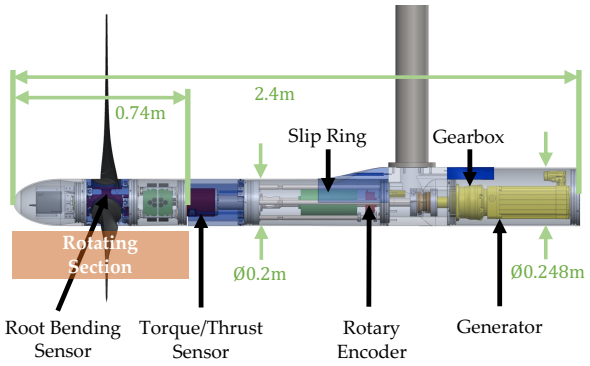

Fig. 6. Overview of mechanical turbine design. Plastic outer shrouding is shown in transparent blue, while the location of rotating section is indicated by the orange bar.

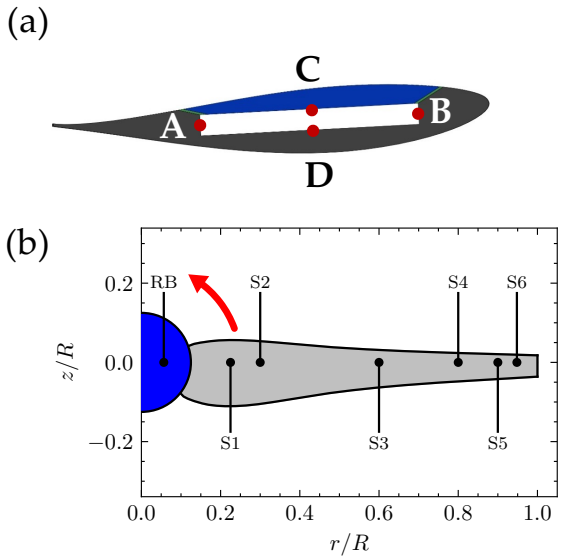

Fig. 7. The strain gauge locations in the blade cross-section at an individual sensor location are shown in (a), while the radial locations of the sensors are plotted in (b) including the location of the Root Bending (RB) sensor.

B. Loads Data

For the data acquired by the turbine, the reduction and processing of the experimental data began with the removal of erroneous spikes and low pass filtering. To remove spikes, all load and angular position data were processed with a Hampel filter with a window length of 20 points. Following this, a fifth order Butterworth low pass filter was applied at $10f_r$ to remove the influence of high frequency noise, where $f_r = \omega/2\pi$ is the rotation frequency.

For the individual blade load sensors, both the root sensors within the hub and the in-blade sensors along the blade span, the combined effect of buoyancy and self-weight generated a periodic component in the measurements that does not relate to the dynamic blade loads associated with operation. To remove this, a simple model was fitted with least squares regression to data obtained with the turbine held stationary at various angular positions. The model considers the response of the sensors to forces both parallel and perpendicular to the blade span. The combined weight and buoyancy signal component can be written as,

$$s_{\mathrm{wl}} = k_2 \sin\theta + k_1 \cos\theta + k_0\,, \tag{6}$$

where s_{wl} denotes the component of the signal relating to buoyancy and self-weight effects, θ defines the angular position of the rotor and k_i are coefficients defined in the least square fitting.

Once filtered and with self-weight and buoyancy effects removed, the calibration curves for the load sensors could be applied to provide measurements in terms of Nm and N. These calibration curves were obtained through an extensive bench testing procedure for the individual blade loads, while provided by the supplier in the case of the Torque-Thrust transducer.

C. Uncertainty Quantification

Uncertainty quantification was undertaken for both the experimental and numerical results. On the experimental side, the ITTC and Equimar guidelines were used as a guide to form the uncertainty estimates. Both the bias and precision uncertainty were included, with the combined uncertainty computed as,

$$u_{\mathrm{D}}^2 = u_{\mathrm{b}}^2 + u_{\mathrm{p}}^2\,, \tag{7}$$

where u_D is the total experimental uncertainty estimate, and u_{b} and u_{p} denote the bias and precision uncertainties respectively.

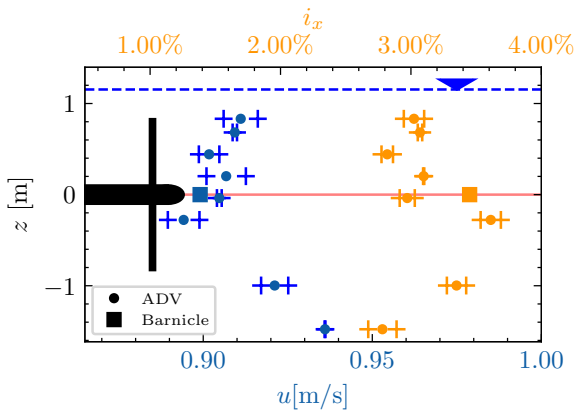

Fig. 8. Flow characterisation of carriage mounted turbulence grid showing the vertical profiles of the mean streamwise velocity and streamwise turbulence intensity. Measurements are taken $5.0\,\mathrm{m}$ downstream of the grid at the position of the rotor plane (without turbine present). The location of the free surface is indicated by the dashed line, while the turbine hub depth is located by the red line, and the rotor extent indicated by the silhouette. All measurement repeats are shown with the solid symbols indicating mean values across the repeats.

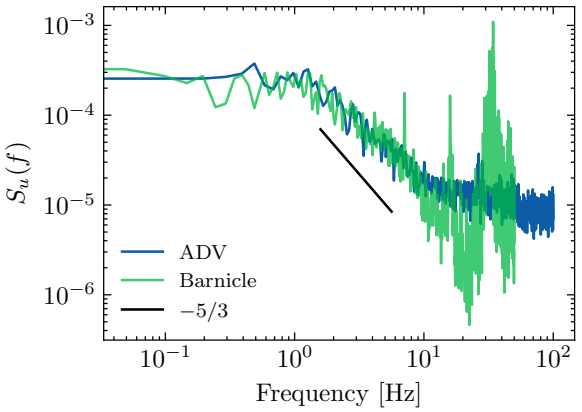

Fig. 9. Flow characterisation of carriage mounted turbulence grid showing the streamwise turbulence spectra with log-log axis scaling.

For the numerical simulations, the uncertainty is estimated following the process in [21], which originates from [22] and [23]. A validation uncertainty is defined as,

$$u_{val}^2 = u_E^2 - u_{model}^2 = u_{num}^2 + u_{input}^2 + u_D^2\,. \qquad (8)$$

The validation process is then described as successful when the comparison error E satisfies the condition of $|E| < u_{val}$. However, two things are to be noted for the present case. Firstly, the input error u_{input} can sometimes be combined with the model error u_{model}, to form a "strong-sense" model as described in [24]. The blade-resolved simulations presented in this paper can be regarded as the strong-sense model, as the only input to the simulation is the inflow conditions and the turbine rotational speed. Secondly, the validation uncertainty u_{val} is plotted separately as u_D on top of the experimental results D and the numerical uncertainty u_{num} on top of the simulation results S.

VI. Results

A. Flow Measurements

The results of the characterisation of the flow downstream of the turbulence grid can be seen in Figs. 8 and 9, showing the vertical velocity profile and the streamwise velocity spectrum respectively. Measurements are taken at the position of the rotor plane which is $5.0\,\mathrm{m}$ downstream of the grid, in the absence of the turbine. The spectra presents a clear $-5/3$ power law decay with close correspondence between results obtained with the Barnacle and ADV probes across the lower frequency range. A pronounced peak is evident in the Barnacle spectra around $\sim$ 30Hz, which is associated with vibration of the towing carriage. Due to the mechanism of operation of the Barnacle probe, it is more susceptible to this form of interference than the ADV probe.

In terms of mean streamwise velocity, the Barnacle provided a value of $0.899\,\mathrm{m/s}$ at hub height, which was slightly below the value obtained with the ADV, at $0.905\,\mathrm{m/s}$, for a carriage towing speed of $1.0\,\mathrm{m/s}$. As the Barnacle was calibrated in-situ against the carriage velocity, this result is considered to be the more robust and is hence used to form the dynamic pressure for all presented non-dimensional quantities (as in Eqn. 9 below). The variation of the mean streamwise velocity in the vertical profile obtained with the ADV was relatively small with less than $0.05U_\infty$ variation within the turbulence grid wake. The onset flow to the downstream turbine is therefore consider to be effectively homogeneous across the rotor frontal area.

Turning to the turbulence statistics, the Barnacle and ADV streamwise turbulence intensities corresponded well, measuring $3.45\,\%$ and $3.1\,\%$ respectively. The integral lengthscales computed from the ADV velocity data were area-averaged over the region occupied by the rotor yielding a value of $0.037\,\mathrm{m}$ for the streamwise velocity component, which is around the same dimension as the blade's tip chord. Although the measured turbulence intensity is lower than original desired, and lower than those pertinent to field applications (circa 10%), the grid elevated turbulence case still provides a robust low turbulence flow condition which, together with modest Reynolds numbers, should ensure post-critical blade flows and therefore provide a relevant test case for model validation for industry applications.

B. Time-Averaged Loads

The loading measurements obtained with the benchmarking turbine are foremost considered in terms of their time averaged values. The performance of the turbine is measured through its power generated, P, and rotor thrust, T, reported as non-dimensional power and thrust coefficients,

$$C_P = \frac{P}{\frac{1}{2}\rho U_\infty^3\,\pi D^2/4} \quad \text{and} \quad C_T = \frac{T}{\frac{1}{2}\rho U_\infty^2\,\pi D^2/4} \qquad (9)$$

and the turbine's power-to-thrust ratio which is indicative of the device's efficiency in extracting energy from the flow. Each flow condition was run three times to ensure repeatability and each time series recorded

around $100 - 200$ revolutions depending on tip-speed ratio and the turbine's rotational frequency.

Fig. 10 demonstrates the integrated quantities with error bars representing a range of $\pm$ two standard errors. The thrust coefficient was found to be 0.876 close to the design operating condition with a tip-speed ratio of 6.03. A small decrease in the thrust coefficient was observed when moving from the low to the elevated turbulence case, although the difference was largely within the estimated experimental uncertainty. When comparing the simulation results to those obtained experimentally, the thrust coefficient was well predicted with a maximum error of $6.3\,\%$ for the elevated turbulence case. This error was smallest close to the design TSR, whilst thrust was over-predicted at both the low and high ends of the TSR sweep.

A peak C_P of 0.485 was observed at a TSR of 5.781 for the clean case, while the peak C_P was found to be slightly reduced for the elevated turbulence case with a value of 0.466 occurring at a TSR of 5.963. The simulations were also found to accurately predict C_P with a maximum error of $10.4\,\%$ occurring at the low end of the TSR sweep, while the error was less than $6\,\%$ over the rest of the TSR range. The greater difference between experiment and simulation at low TSRs is likely attributed to the increasing influence of flow separation and stall at low TSRs, recalling in particular that the simulations are steady which will adversely effect predictions at low TSRs. Additionally, the simulation results also demonstrated a drop in performance with elevated turbulence, although this was not as pronounced as observed in the experiments. The authors attribute the small over-prediction of C_P to surface roughness effects, with the experimentally recorded torque reduced by an increased shear stress on the blade surface.

The turbine exhibits a high power-to-thrust ratio inferring efficient extraction of energy from the stream. The ratio of power-to-thrust coefficients, also referred to as the basin efficiency, is the ratio of generated power to power removed from the flow, with the latter including the necessary power required to remix the turbine's core flow with the flow bypassing it as it recovers to a homogenised flow condition. The basin efficiency infers how well the tidal resource is being utilised and it is important that it is maximised in commercial applications so that the total energy extraction from the scarce tidal resource is maximised. In unblocked flow a turbine performing at the Betz limit of power extraction, $C_P = 16/27$, has a basin efficiency of $C_P/C_T = 2/3$. We conclude that at the benchmarking turbine's operating point for maximum power coefficient, the turbine, with a power-to-thrust coefficient ratio of 0.54, is performing at around 81% of the maximum achievable efficiency in unblocked flow.

The time-averaged bending moments evaluated by the in-blade sensors and root bending sensors are illustrated in Fig. 11. The diagrams at the top of the figure represent the locations of the sensors and the regions of the blade contributing to the measured bending moments for each of the measurement locations. The bending moments are shown in their non-dimensional form, which is defined as,

$$C_{\mathrm{BM}} = \frac{M}{\frac{1}{2}\rho U_\infty^2 \pi D^3/8}, \tag{10}$$

where M denotes the bending moment. Bending moments are accumulative along the blade span and hence very different in magnitude at root and tip, and care must be taken when comparing values across the span, and in interpreting the significance of differences between simulations and experiments.

The variation of the flapwise bending moments follows similar trends with TSR to the thrust coefficient at all the measured radial locations. The edgewise bending moment presents a similar trend with TSR to torque across the inboard and mid-span regions, whilst at $0.8R$ and outboard the trend is flatter in nature. By linearly interpolating the bending moments obtained in elevated turbulence conditions with tip-speed ratio, they can be directly compared to the low turbulence case values. This analysis demonstrates only a very small influence of the grid generated turbulence, with the absolute percentage difference based on the low turbulence case bounded by $2\,\%$ and $9\,\%$ in the flapwise and edgewise directions respectively, which is largely within the experimental uncertainty.

Comparing the experimental and simulated flapwise bending moments, the difference is found to be smallest just below the design operating condition at a TSR of 5.5. In the radial direction, the differences between simulation and experiment were consistently smallest at the $0.6R$ radial position for both the low and elevated turbulence cases. This suggests that differences between the experimental and simulated flapwise bending moments were largely driven by root and tip effects. The greatest differences occurred in the tip region, with the simulations under-predicting the flapwise bending moment by up to $19\,\%$ at $r = 0.9R$. In the edgewise direction, the difference between simulation and experiment was smallest at the root with the difference growing consistently towards the tip measurements. The edgewise bending moments at the $0.8R$ and $0.9R$ locations were highly under-predicted by the simulations.

Although there are significant differences in the simulated and experimental bending moments in the tip region, the bending moments here are very small, and consequently these differences have little impact on the accuracy of root bending moment predictions. We further note that for both the flapwise and edgewise bending moments to be under-predicted in the tip region requires a drop in the blade lift force in this region which could be caused by a reduction in the local angle-of-attack. Whilst the rotor blades were simulated as rigid, they do of course deflect and twist experimentally. We postulate that the experimental blades twisted in the tip region so as to increase the local of angle-of-attack, leading to the out of trend variation in the outboard edgewise bending moment with TSR, and the divergence between simulated and experimental data over the outboard section of the blade $r/R \geq 0.8$. Uncoupled Finite Element Analysis of the blade's deformation under the simulated loading

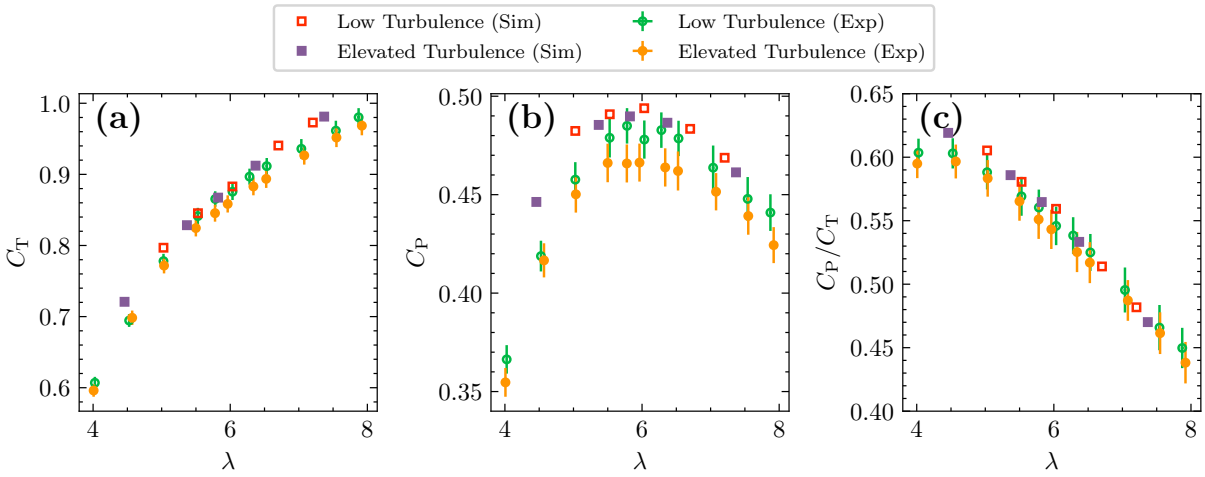

Fig. 10. (a) and (b) Thrust and power coefficients, and (c) power-to-thrust ratio with tip-speed ratio. The error bars indicate the 95 % confidence interval based on the total estimated uncertainty with circles representing experimental results and simulated results shown with squares.

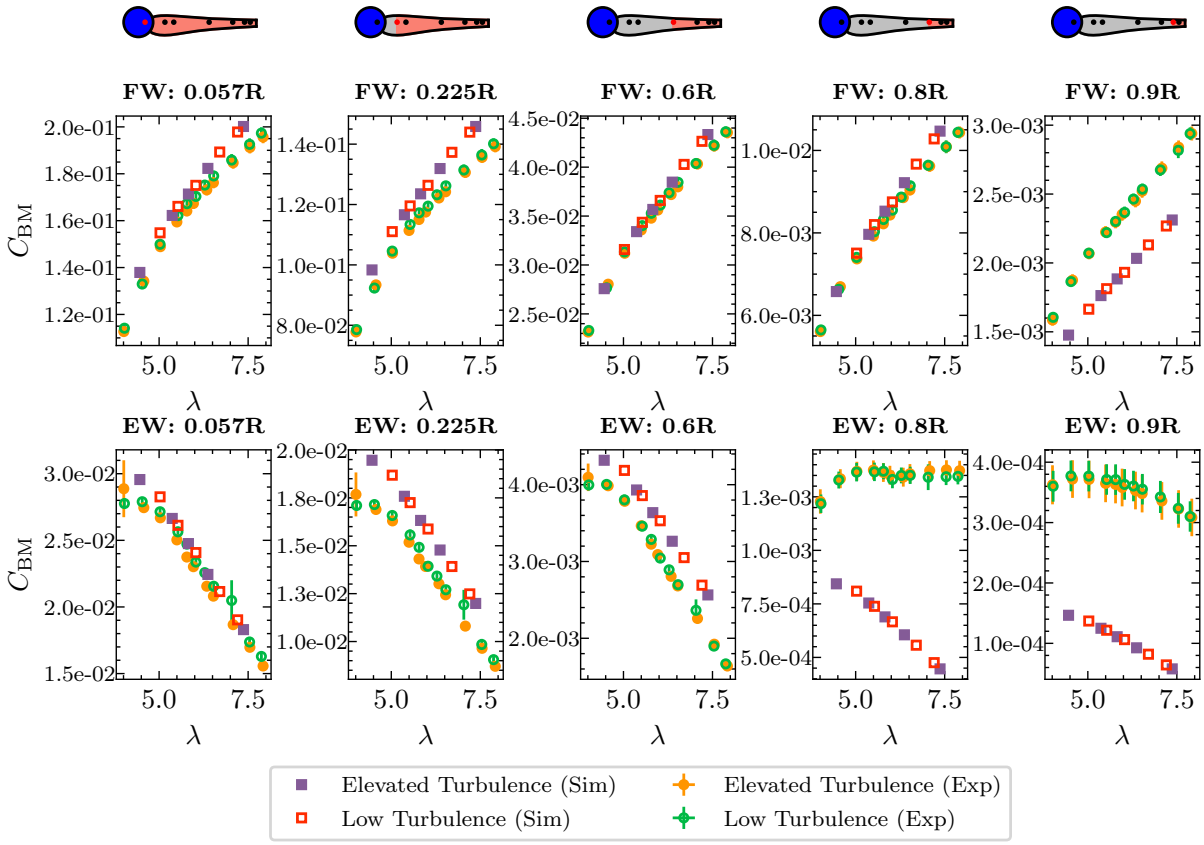

Fig. 11. Bending moment coefficients, C_{BM}, across the tip-speed ratio sweep for both experiments and simulations at low and elevated turbulence levels. Flapwise (FW) and edgewise (EW) bending moments are presented in the top and bottom rows respectively, with the blade diagrams at the top of the figure indicating the locations of the sensors and the shaded portions representing the regions of the blade contributing to the bending moments at each of the measurement locations. Note the very different ranges of C_{BM} in sub-plots between blade tip and root.

distribution (not presented) confirms the direction and magnitude of the implied angle-of-attack change in this region.

VII. Conclusions

A 1.6m diameter laboratory-scale experimental tidal turbine was designed, developed and tested in a large towing tank facility for the purpose of providing validation data for a subsequent blind benchmarking programme. The turbine operated in a post-critical Reynolds number regime with low global blockage and well-defined flow conditions, thus providing relevant data for validating models intended for use in the design and analysis of full-scale turbines.

High fidelity load measurements were obtained with in-blade instrumentation to measure edgewise and flapwise bending moments at several locations along the blade span, together with blade root bending mo-

ments and overall rotor thrust and torque. Both a low turbulence and elevated turbulence test case (3.1% turbulence intensity) were considered with the latter being achieved by pushing a turbulence generation grid ahead of the test turbine.

The design simulations were found to accurately predict the thrust and power coefficient for both the low and elevated turbulence cases. The experimental results demonstrated only a small decrease in the power coefficient with the elevation of the turbulence level. Comparison of the experimental in-blade bending moments with the design simulation demonstrated good agreement with small departures in the root and tip regions. A significant difference, but of small magnitude and little overall consequence on root bending moments, occurs in the tip region. We associate this with the angular deflection of the blade under load, that is not represented in the rigid blade simulations.

ACKNOWLEDGEMENT

This benchmarking exercise is funded by the Supergen ORE Hub, grant number EP/S000747/1, and by RHJW's EPSRC Advanced Fellowship EP/R007322/1. We would like to thank Catherine Wilson at the University of Cardiff for loan of ADV equipment. The authors are also grateful for the assistance of QinetiQ staff during the testing campaign. The authors would also like to acknowledge the use of the University of Oxford Advanced Research Computing (ARC) facility in carrying out the computational part of this work. http://dx.doi.org/10.5281/zenodo.22558

REFERENCES

[1] A. Bahaj, W. Batten, and G. McCann, "Experimental verifications of numerical predictions for the hydrodynamic performance of horizontal axis marine current turbines," *Renewable Energy*, vol. 32, no. 15, pp. 2479–2490, 2007. [Online]. Available: https://www.sciencedirect.com/science/article/pii/S0960148107002996

[2] B. Gaurier, G. Germain, J. Facq, C. Johnstone, A. Grant, A. Day, E. Nixon, F. Di Felice, and M. Costanzo, "Tidal energy "round robin" tests comparisons between towing tank and circulating tank results," *International Journal of Marine Energy*, vol. 12, pp. 87–109, 2015, special Issue on Marine Renewables Infrastructure Network. [Online]. Available: https://www.sciencedirect.com/science/article/pii/S2214166915000223

[3] G. S. Payne, T. Stallard, and R. Martinez, "Design and manufacture of a bed supported tidal turbine model for blade and shaft load measurement in turbulent flow and waves," *Renewable Energy*, vol. 107, pp. 312–326, 2017. [Online]. Available: https://www.sciencedirect.com/science/article/pii/S0960148117300782

[4] B. Gaurier, M. Ikhennicheu, G. Germain, and P. Druault, "Experimental study of bathymetry generated turbulence on tidal turbine behaviour," *Renewable Energy*, vol. 156, pp. 1158–1170, 2020. [Online]. Available: https://www.sciencedirect.com/science/article/pii/S0960148120306340

[5] L. Luznik, K. A. Flack, E. E. Lust, and K. Taylor, "The effect of surface waves on the performance characteristics of a model tidal turbine," *Renewable Energy*, vol. 58, pp. 108–114, 2013. [Online]. Available: https://www.sciencedirect.com/science/article/pii/S0960148113001316

[6] R. Willden, X. Chen, S. T. Harvey, H. Edwards, C. Vogel, K. Bhavsar, T. Allsop, J. Gilbert, H. Mullings, M. Ghobrial, P. Ouro, D. Apsley, T. Stallard, I. Benson, A. Young, P. Schmitt, F. Z. de Arcos, M.-A. Dufour, C. C. Bex, G. Pinon, A. Evans, M. Togneri, I. Masters, L. da Silva Ignacio, C. Duarte, F. Souza, S. Gambuzza, Y. Liu, I. Viola, M. Rentschler, T. Gomes, G. Vaz, R. Azcueta, H. Ward, F. Salvatore, Z. Sarichloo, D. Calcagni, T. Tran, H. Ross, M. Oliveira, R. Puraca, and B. Carmo, "Tidal turbine benchmarking project: Stage I - Steady flow blind predictions," in *Proceedings of the 15th European Wave and Tidal Energy Conference*, 2023.

[7] A. M. Young, N. R. Atkins, C. J. Clark, and G. Germain, "An unsteady pressure probe for the measurement of flow unsteadiness in tidal channels," *IEEE Journal of Oceanic Engineering*, vol. 45, no. 4, pp. 1411–1426, 2020.

[8] Alstom, "Alstom's 1mw tidal stream turbine installed in scotland achieves 1 gwh power production," Alstom Press Release and News, 2014, [Online, accessed 2nd June 2021]. [Online]. Available: https://www.alstom.com/press-releases-news/2014/12

[9] A. Wimshurst and R. H. J. Willden, "Computational observations of the tip loss mechanism experienced by horizontal axis rotors," *Wind Energy*, vol. 21, no. 7, pp. 544–557, 2018.

[10] F. Zilic de Arcos, C. R. Vogel, and R. H. J. Willden, "Extracting angles of attack from blade-resolved rotor cfd simulations," *Wind Energy*, vol. 23, no. 9, pp. 1868–1885, 2020.

[11] C. R. Vogel and R. H. J. Willden, "Investigation of wind turbine wake superposition models using reynolds-averaged navier-stokes simulations," *Wind Energy*, vol. 23, no. 3, pp. 593–607, 2020.

[12] L. Deng, Z. Qiao, X. Yang, and J. Xiong, "Aerodynamics performance computational of trailing-edge-blunting methods of flatback airfoil for large wind turbine based on rans equation," *Acta Energiae Solaris Sinica*, vol. 33, no. 4, pp. 545–551, 2012.

[13] J. McNaughton, B. Cao, S. Ettema, F. Z. de Arcos, C. Vogel, and R. Willden, "Experimental testing of the performance and interference effects of a cross-stream array of tidal turbines," in *Developments in Renewable Energies Offshore, Proceedings of the 4th International Conference on Renewable Energies Offshore*, 2020.

[14] C. Bak, P. Fuglsang, J. Johansen, and I. Antoniou, "Wind tunnel tests of the naca 63-415 and a modified naca 63-415 airfoil," in *RISØ-R–1193*, 01 2000.

[15] H. Cerón-M, F. Catalano, and A. C. Filho, "Experimental study of the influence of vortex generators on airfoils for wind turbines," in *Conference: VI Congreso Internacional de Ingeniería Mecánica*, 05 2013.

[16] M. Parsheh, F. Sotiropoulos, and F. Porté-Agel, "Estimation of power spectra of acoustic-doppler velocimetry data contaminated with intermittent spikes," *Journal of Hydraulic Engineering*, vol. 136, no. 6, pp. 368–378, 2010.

[17] J.-B. Richard, J. Thomson, B. Polagye, and J. Bard, "Method for identification of doppler noise levels in turbulent flow measurements dedicated to tidal energy," *International Journal of Marine Energy*, vol. 3-4, pp. 52–64, 2013, special Issue – Selected Papers - EWTEC2013.

[18] S. Pope, *Turbulent Flows*. United Kingdom: Cambridge University Press, 2014.

[19] P. L. O'Neill, D. Nicolaides, D. R. Honnery, and J. Soria, "Autocorrelation Functions and the Determination of Integral Length with Reference to Experimental and Numerical Data," in *Proceedings of the 15th Australasian Fluid Mechanics Conference*, Sydney, Australia, 2004.

[20] T. Blackmore, L. E. Myers, and A. S. Bahaj, "Effects of turbulence on tidal turbines: Implications to performance, blade loads, and condition monitoring," *International Journal of Marine Energy*, vol. 14, pp. 1–26, 2016.

[21] ASME V&V 20, *Standard for Verification and Validation in Computational Fluid Dynamics and Heat Transfer*. ASME, 2009.

[22] H. W. Coleman and F. Stern, "Uncertainties and CFD Code Validation," *Journal of Fluids Engineering*, vol. 119, no. 4, pp. 795–803, 12 1997.

[23] H. W. Coleman and W. G. Steele, "Engineering application of experimental uncertainty analysis," *AIAA Journal*, vol. 33, no. 10, pp. 1888–1896, 1995.

[24] C. J. Freitas, "Standards and Methods for Verification, Validation, and Uncertainty Assessments in Modeling and Simulation," *Journal of Verification, Validation and Uncertainty Quantification*, vol. 5, no. 2, 06 2020.